JACS
JOURNAL OF THE AMERICAN CHEMICAL SOCIETY
pubs.acs.org/JACS

Article

Assembly of Face Decorated Cuboidal Cages into Ultraporous Structures with Hierarchical Porosity: Accessing MOFs with the Awaited red-a Topology

Konstantinos G. Froudas, Constantinos Tsangarakis, Tamsyn Montagnon, Charalampos Livas, Emmanuel Klontzas, George E. Froudakis, Christos Tampaxis, Georgia Charalambopoulou, Theodore A. Steriotis, and Pantelis N. Trikalitis*

Cite This: https://doi.org/10.1021/jacs.5c16581

Read Online

ACCESS | Metrics & More | Article Recommendations | Supporting Information

ABSTRACT: The rational design of ultraporous metal−organic frameworks (MOFs) with hierarchical pore systems is of great significance but remains highly challenging. MOFs based on the **reo-e** or **red** topologies offer such pore architectures through face-shared cuboidal, cuboctahedral, and rhombicuboctahedral cages. Although hypothesized and computationally explored over the past two decades, these solids had not been experimentally realized. Here, we report the first MOFs based on the long-awaited **red-a** net, denoted as M-**red**-MOF-1 (M = Fe, Cr). Combining the nearly square yet rectangularly connected 4-c organic linker 4,4′,″,4‴-([1,1′:4′,1″-terphenyl]-3,3′′,5,5′′-tetrayltetrakis(ethyne-2,1-diyl))tetrabenzoic acid, denoted as H_4TCEPT, with $FeCl_3 \cdot 6H_2O$ under solvothermal conditions yielded Fe-**red**-MOF-1 as cubic-like single crystals. Extensive characterization using SCXRD, PXRD, SEM, TEM, gas sorption, TGA, and in-silico structure modeling, confirmed the **red-a** topology. Argon sorption at 87 K revealed three distinct S-type steps, consistent with the hierarchical pore network and demonstrated an ultrahigh pore volume (3.56 $cm^3\ g^{-1}$) and BET area (5081 $m^2\ g^{-1}$). Owing to its hierarchical porosity, Fe-**red**-MOF-1 exhibits excellent hydrogen storage performance with high gravimetric (13.5 wt %) and volumetric (39.5 $g{\cdot}L^{-1}$) working capacities under temperature and pressure swing conditions (77 K/100 bar → 160 K/5 bar), placing it among the top-performing MOFs. The isostructural Cr-**red**-MOF-1, obtained postsynthetically, showed a remarkable water uptake of 2.81 g g^{-1} at 298 K, surpassing the current top-ranking Cr-**soc**-MOF-1 (1.95 g g^{-1}). Isoreticular analogues, denoted as M-**red**-MOF-2 (M = Fe, Cr), were also synthesized using the anthracene-based linker H_4TEBDA. The present work opens new directions for designing ultraporous, hierarchical MOFs based on the **red-a** net.

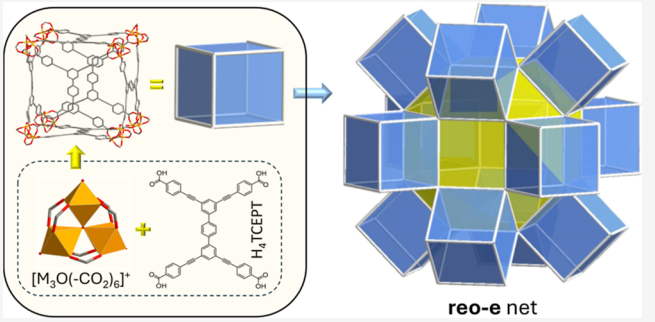

INTRODUCTION

Metal−organic frameworks (MOFs) are an important class of functional porous materials with a highly modular nature, as their assembly from molecular inorganic and organic building blocks (MBBs) can be rationally controlled according to the principles of reticular chemistry.[1−6] While extensive work has been done on fine-tuning established network topologies through the delicate practice of different approaches including isoreticular expansion/contraction or ligand functionalization among others, numerous novel, hypothetical MOF structures, with great potential in real-world applications have been proposed over the years.[7−12] In most cases, the computational generation of these hypo-nets relies on the augmentation of known, predominantly high-symmetry structures (e.g., mineral structures or zeolite nets), or on the assembly of metal−organic polyhedra (MOPs) as supermolecular building blocks (SBBs), based on symmetry-rich architectures, as well as on the reticulation of edge-transitive nets and their expanded edge-net analogues.[9,13,14] In addition, Eddaoudi et al. proposed recently the merged-nets approach for the systematic design of hypothetical, multicomponent MOFs, as appropriate blueprints.[8] Some of the above hypothetically proposed MOFs have been accessed through exploratory synthesis or deliberate design;[8,15−18] nevertheless, a large number remains experimentally unrealized. This can be attributed to different factors depending on the targeted hypo-topology including: (i) the demand for intricate, well-defined building blocks, whose

Received: September 21, 2025
Revised: December 4, 2025
Accepted: December 15, 2025

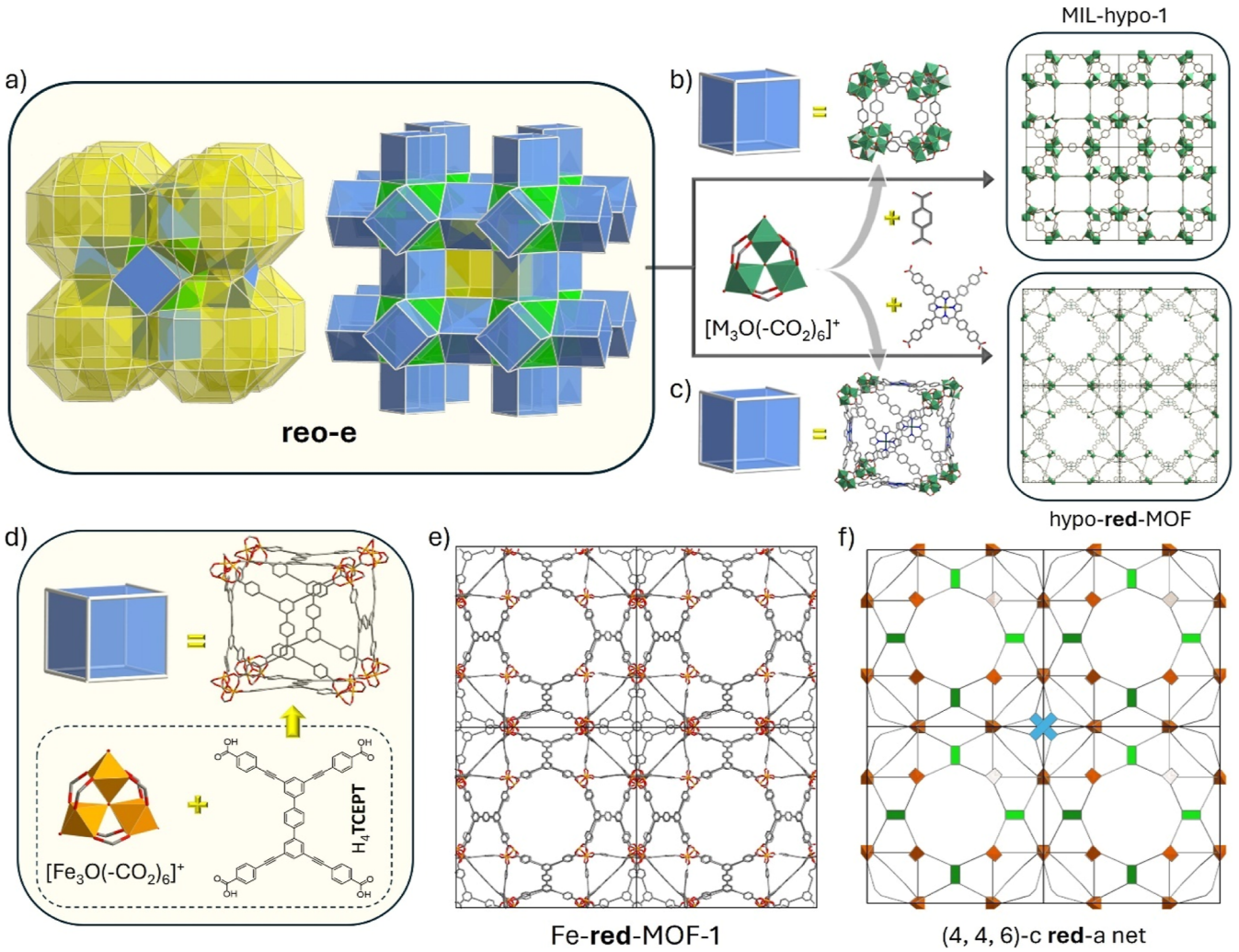

Figure 1. (a) The **reo-e** network shown at the left as a primitive cell of face-shared large rhombicuboctahedra (yellow) and at the right, as a packing of corner-shared cubes. In both cases, the different polyhedral cavities that are formed are shown with different colors (green: cuboctahedra, blue: cubes). (b) The hypothetical structure of **MIL-hypo-1** proposed by Férey et al., in which the cubes are made by 6-c trigonal prismatic $[Cr_3(\mu_3\text{-}O)(-COO)_6]^+$ MBBs occupying the corners, bridged by ditopic 1,4 benzene dicarboxylate (BDC) linkers lying at the edges. (c) The hypothetical structure hypo-**red**-MOF proposed by Eddaoudi et al., where the faces of the cubes are occupied by a porphyrin-derived, 4-c square carboxylate linker. (d) The use of 4-c H_4TCEPT linker in combination with 6-c $[Fe_3(\mu_3\text{-}O)(-COO)_6]^+$ MBBs resulted in face-decorated cuboidal cages. (e) The cubic structure of Fe-**red**-MOF-1 looking down the *a*-axis. (f) The unique trinodal, (4,4, 6)-c, augmented **red-a** net derived from the topological analysis of Fe-**red**-MOF-1. Note the two crystallographically distinct 4-c linkers, represented with green and blue (at the center) colors.

embedded structural information serves to precisely code the targeted net, by solely matching its vertex figures or (ii) the competition with other more kinetically stable or more symmetric nets being formed by the same building block combination.

Following the report of the iconic MIL-100, an ultraporous MOF displaying the **mtn**/**moo-a** topology, derived by the eclipsed corner-sharing packing of supertetrahedra (ST) as SBBs,[19] Férey et al. proposed a series of hypothetical, computationally designed frameworks.[20] While in the case of MIL-100, the STs are constructed by 6-connected trigonal prismatic, trinuclear $[Cr_3(\mu_3\text{-}O)(-COO)_6]^+$ carboxylate-based clusters as vertices and 1,3,5 benzene tricarboxylate (BTC) as faces, it has been suggested that these inorganic metal-oxo trimers (M_3O) can also be connected with 1,4 benzene dicarboxylate (BDC) to form either supertetrahedra or supercubes (SC), as SBBs.[20] In both configurations, the corners of the SBBs are occupied by the trimeric MBBs, while the ditopic linkers are placed at the edges. Shortly after, the computationally generated ST was experimentally realized through the synthesis of MIL-101, which features the **mtn-e-a** topology-displaying the same ST packing as observed in MIL-100.[21] In addition to the computational design of SCs and STs as novel SBBs, Férey also proposed their subsequent assembly into three-dimensional (3D) frameworks, inspired by previously reported architectures, derived from the space filling packing of polyhedra. In particular, O'Keeffe described a packing arrangement of polyhedra including rhombicuboctahedra and cubes, in a way that a continuous 3D tilling is achieved (Figures 1a and S19).[22] Importantly, in this configuration, cubic polyhedra are directly connected at their corners, enabling the conceptual development of a hypothetical network, namely **MIL-hypo-1**, in which the cubic polyhedra are replaced by the computationally generated SCs and rhombicuboctahedra are considered as voids (Figure 1b). The resulting 3D framework, generated by the corner sharing arrangement of cubic SBBs can also by simplified as the **reo** edge net (**reo-e**), displaying an impressive hierarchical pore

https://doi.org/10.1021/jacs.5c16581
J. Am. Chem. Soc. XXXX, XXX, XXX−XXX

system, composed of cuboctahedral and rhombicuboctahedral cages, while it is important to highlight that the cubic SBBs function as porous cages as well (Figures 1a and S20). Likewise, derived from *a* space filling packing of cubes, tetrahedra and rhombicuboactahedra, **MIL-hypo-2** was introduced as hypothetical net with a novel network topology, emerged by the corner-sharing alternating arrangement of the previously mentioned SC and ST SBBs, identical to the arrangement found in **flu-e** net. Although the long-anticipated structure of **MIL-hypo-2** was materialized with the discovery of MCF-35, to the best of our knowledge, **MIL-hypo-1** (**reo-e**) remains unreported for more than 20 years.[23] The reported multicomponent MOF with a chemical formula $(Ni_3O)_2Ni(H_2O)_2(BDC)_6(na)_4$ (na: nicotinic acid) is not a **reo-e** type structure, but a merged 3p-0p network, according to the recent work by Eddaoudi and co-workers, resulting from the coordinative encapsulation of zero-periodic (0p) $Ni_{12}(na)_{24}$ cuboctahedra into the rhombicuboctahedral cages of a three-periodic (3p) $(Ni_3O)(BDC)_3$ **reo-e** net (Figure S21).[8,24] To an extent, the absence of **MIL-hypo-1** type structures so far can be attributed to the versatility in the possible outcome nets from the combination of the 6-c, trimeric MBBs and ditopic ligands, including the well-known **acs**- and **mtn-e**-MOFs.[21,25,26] Even if the reaction conditions that drive the formation of specific SBBs could have been identified, it is still challenging to dictate their assembly into a 3D framework. More recently, Eddaoudi and co-workers proposed a face decoration strategy on a series of edge nets, including **reo-e** net.[10] More specifically, a hypothetical **MIL-hypo-1** type structure was introduced, where the cubic SBBs are formed by inorganic metal-oxo trimers as corners and 4-connected, square-like ligands as faces (Figure 1c).[10] It is important to emphasize that the generated (4, 4, 6)-c net displaying the **red-a** topology is differentiated from the (4, 6)-c **soc-a** net on the way that the cubic SBBs are assembled. In particular, both network topologies emerge from the corner sharing arrangement of cubic SBBs. While in **soc-a** net a staggered motif is identified,[27] the formation of the hypothetical **red-a** topology demands an eclipsed corner sharing packing of cubes, which has only been observed in the case of Fe-**tbb**-MOFs, previously reported by our group.[28]

In our continuous efforts to apply reticular chemistry for the construction of ultraporous MOFs and considering the important gas storage properties of **soc** and **tbb**-based MOFs, including H_2 and CH_4, we initiated an exploratory synthesis using expanded 4-c carboxylate-based organic linkers such as the 4,4′,4″,4‴-([1,1′:4′,1″-terphenyl]-3,3′′,5,5′′-tetrayltetrakis(ethyne-2,1-diyl))tetrabenzoic acid, denoted as H_4TCEPT. Remarkably, the solvothermal reaction of H_4TCEPT with $FeCl_3{\cdot}6H_2O$ afforded cubic-like single crystals, denoted as Fe-**red**-MOF-1, exhibiting the awaited (4, 4, 6)-c **red-a** topology. The fact that H_4TCEPT did not afford a MOF with the **soc-a** topology, as has been considered and constructed computationally[27] but never reported experimentally, prompted us to examine carefully the **soc-a** and **red-a** nets and understand why in this case the **red-a** structure is formed. As we explain in detail in the next section, the particular geometric characteristics of the 4-c H_4TCEPT ligand, being nearly square but with an off-diagonal displacement of the carboxylate groups, described as a rectangular 4-c connectivity, play an important role in stabilizing the **red-a** topology, providing key design principles for the reticular synthesis of MOFs with this unique topology. Argon sorption measurements at 87 K on supercritical CO_2-activated Fe-**red**-MOF-1 revealed a unique three-step sorption isotherm, consistent with the hierarchical nature of the **red-a** net, and yielded an ultrahigh total pore volume of 3.56 $cm^3{\cdot}g^{-1}$ and a BET area of 5081 $m^2{\cdot}g^{-1}$, placing this material among the top ultraporous MOFs.[15,29−32] Because of the exceptional porosity, Fe-**red**-MOF-1 was investigated for H_2 storage at cryogenic conditions, revealing a remarkable performance. Finally, following a topotactic metal cation exchange reaction, we obtained the Cr-analogue, denoted as Cr-**red**-MOF-1 which is found stable in open air for at least a month. Notably, Cr-**red**-MOF-1 demonstrates a record high water adsorption at 298 K reaching an astonishing uptake of 2.81 g g^{-1} at 95% RH, which is significantly higher compared to the currently top-ranking Cr-**soc**-MOF-1 (1.95 g g^{-1}).[33] To further enrich the family of these important MOFs, we applied reticular chemistry and successfully synthesized Fe-**red**-MOF-2 using the anthracene-based linker 4,4′,4″,4‴-((anthracene-9,10-diylbis(benzene-5,1,3-triyl))tetrakis(ethyne-2,1-diyl))tetrabenzoic acid, denoted as H_4TEBDA. The isostructural Cr-**red**-MOF-2 was also prepared via topotactic transmetalation from the parent Fe-**red**-MOF-2.

RESULTS AND DISCUSSION

In the quest for highly porous MOFs for gas storage applications, the reticular synthesis of Al-**soc**-MOF-1 based on the 4-c 3,3″,5,5″-tetrakis(4-carboxyphenyl)-*p*-terphenyl (H_4TCPT) rectangular linker and related materials by the Eddaoudi group, represents an important milestone, as they offer very high uptakes with balanced gravimetric and volumetric working capacities.[27] This important family of MOFs offers great opportunities for further development of materials with optimized properties through linker expansion and decoration. Accordingly, different expanded variants of H_4TCPT linkers, including H_4TCEPT which is formed by replacing the benzoic acid groups with 4-ethynylbenzoic acid moieties, were used computationally to construct in-silico Al-based **soc**-type MOFs and evaluate their performance in CH_4 storage.[27] In our group, we targeted the synthesis of **soc**-type MOFs based on expanded linker analogues and within this context we initiated an exploratory synthesis using the H_4TCEPT linker. Interestingly, the isolation of a crystalline product was not straightforward, and the synthesis protocol of Al-**soc**-MOF-1 resulted in an amorphous solid. Based on our long-standing experience with MOFs constructed from trinuclear oxo-centered clusters, we focused on Fe^{3+} instead of Al^{3+} because the former is more kinetically labile and has reduced metal−carboxylate bond strength due to its softer Lewis acidity, which increases bond reversibility and facilitates error correction during self-assembly, thereby promoting the formation of crystalline products with the H_4TCEPT linker. Indeed, after extensive synthetic work, the reaction of $FeCl_3{\cdot}6H_2O$ with H_4TCEPT in diethylformamide (DEF) in the presence of tetrafluoroboric acid acting as modulator afforded orange, cubic crystals, denoted as Fe-**red**-MOF-1. Attempts to collect single crystal data using an in-house single crystal X-ray diffraction (SCXRD) instrument resulted in a very weak diffraction allowing only unit cell determination, revealing a cubic lattice with a cell parameter of 52.24 Å (Figure S29). This was surprising because the expected unit cell size for a **soc**-type structure based on the H_4TCEPT linker was expected to be significantly smaller. This is confirmed by constructing in-silico the expanded **soc** MOF, denoted as Fe-**soc**-TCEPT,

https://doi.org/10.1021/jacs.5c16581
J. Am. Chem. Soc. XXXX, XXX, XXX−XXX

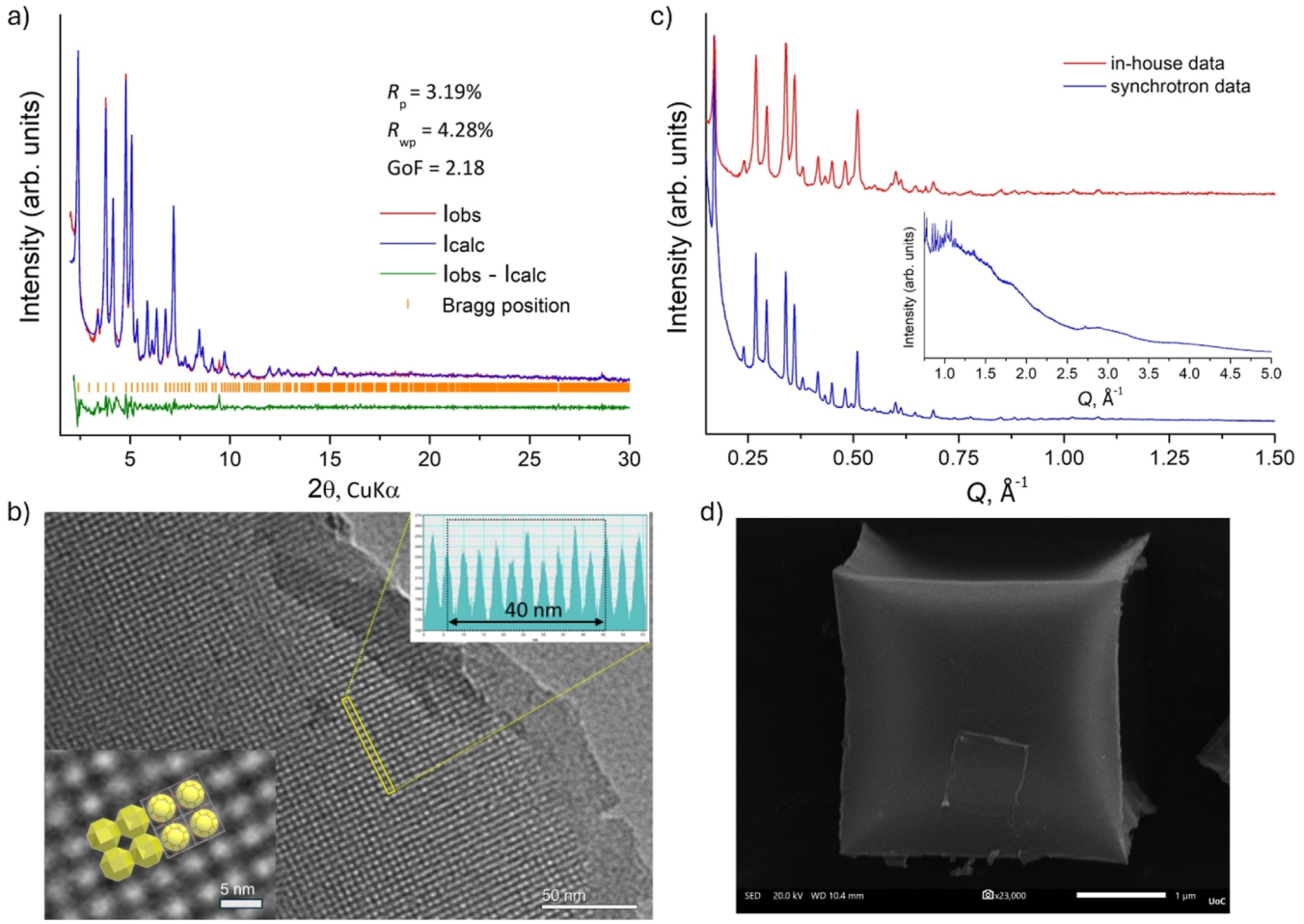

Figure 2. (a) Experimental PXRD pattern (red line) and calculated profile from the Le Bail refinement (blue line) for Fe-**red**-MOF-1 in the space group *Pm*-3*m*. (b) Representative TEM image of activated Fe-**red**-MOF-1 1 revealing a square-like periodicity of mesopores. Top-right inset shows the intensity profile of the yellow rectangular box from which the mesopore-to-mesopore distance, averaged over 10 peaks, is 40 Å. Shown in the bottom-left inset are the primitive cubic packing of the large rhombicuboctahedral mesoporous cages (yellow) and the corresponding unit cells of Fe-**red**-MOF-1, superimposed on the observed square-like periodicity. (c) High resolution PXRD pattern of activated Fe-**red**-MOF-1 recorded using synchrotron radiation (blue line) as compared to the corresponding pattern obtain by an in-house instrument (red line). (d) Representative SEM image of a single cuboidal particle of activated Fe-**red**-MOF-1 showing the curved faces.

where the optimized unit cell has an edge length of 43.32 Å (Figure S22a). Importantly, the powder X-ray diffraction (PXRD) pattern of the as-synthesized Fe-**red**-MOF-1 revealed multiple Bragg reflections in the low angle region (<10 deg 2theta), which are not expected for a **soc**-type structure (Figure S33). This is because the reported experimental PXRD pattern of Fe-**soc**-MOF-1, based on the H_4TCPT linker, shows only a few reflections in this low-angle region, and for an isoreticular expanded analogue, a very similar pattern would be expected, with the Bragg peaks shifted toward lower 2θ angles. A comparison of the calculated PXRD pattern of the in-silico constructed Fe-**soc**-TCEPT with the experimental pattern of Fe-**red**-MOF-1, shown in Figure S33, reveals that these are very different, strongly suggesting that the latter corresponds to a distinct structure. It is noted that in Fe-**soc**-TCEPT, the linker is distorted (Figure S22b), with the angle between adjacent benzoate groups deviating noticeably from the ideal 120° to 111°, implying that this linker does not fit well and therefore, may not be suitable for the construction of a **soc-a** net. As we discuss below, the **soc-a** net requires a rectangular rather than a square linker (Figure S25a). The H_4TCEPT linker has a nearly square shape and therefore in Fe-**soc**-TCEPT is forced to adopt a rectangular geometry. In turn, because the linker distortion is associated with an energy penalty, it is natural to consider this as the reason why Fe-**soc**-TCEPT is not formed under the particular reaction conditions.

To unambiguously determine the crystal structure of Fe-**red**-MOF-1, we submitted as-made samples for SCXRD measurements using synchrotron radiation as well as in state-of-the-art electron diffractometers, but with no success in all cases. We decided to prepare a solvent free Fe-**red**-MOF-1 to significantly increase the electron density contrast and enhance the intensity of the diffracted Bragg peaks. To receive the best quality activated material, we used supercritical CO_2 ($scCO_2$) under flow conditions in an ethanol exchanged sample, using a custom-made apparatus (Figure S61). Indeed, the intensity of the low angle Bragg peaks in the PXRD pattern of activated Fe-**red**-MOF-1 was significantly increased compared to the as-made (solvent containing) solid, as shown in Figures 2a,c and S34. This good quality PXRD pattern was successfully indexed to a primitive cubic unit cell with a refined parameter of 52.22(3) Å, in full agreement with the unit cell obtained experimentally from the SCXRD measurements, indicating the formation of a phase pure solid (Figures S35 and S36, Table

https://doi.org/10.1021/jacs.5c16581
J. Am. Chem. Soc. XXXX, XXX, XXX−XXX

S3). In parallel, we performed an argon sorption measurement at 87 K to evaluate the porosity of this material. Remarkably, a unique multistep isotherm was recorded, with an ultrahigh adsorption uptake of 2798 cm^3(STP) g^{-1} at 0.99 p/p_0 which corresponds to a total pore volume of 3.56 cm^3 g^{-1} (Figure 4c). In particular, three distinct S-type steps are observed in the isotherm, associated with three different pore sizes (Figure 4c). The first step is completed around 0.15 p/p_0, the second at 0.25 p/p_0 and the third sharp, capillary condensation step slightly above 0.4 p/p_0, associated with the presence of relatively large mesopores. In fact, the desorption curve revealed a small but clear hysteresis for this high relative pressure step, which is consistent with the presence of mesopores close to 40 Å associated with a delayed condensation during adsorption. The calculated BET area, following the consistency criteria (selected relative pressure range: 0.12−0.18 p/p_0), was found to be 5081 m^2 g^{-1} (Figure S45).[34] Attempts to perform pore size distribution (PSD) analysis using available DFT models applied on the whole isotherm did not result in acceptable fits (Figure S48). Interestingly, an excellent fit was obtained by excluding the low-pressure region up to 0.1 p/p_0 (Figure S47). The corresponding PSD curve shows two peaks centered at 41.2 and 29.6 Å which as we describe below are consistent with the crystal structure (Figure 4c). The fact that it was unable to find a suitable model to fit the low-pressure region (<0.1 p/p_0), where pores up to approximately 20 Å are filled, could be associated with the unusual shape of the isotherm until the first knee observed at around 0.1 p/p_0. More specifically, for rigid pores in the range 4−20 Å, the isotherm is typically concave with respect to the p/p_0 axis, where in our case a convex shape is observed.[35] For example, in PCN-333(Fe, Al), which possesses a rigid hierarchical pore system with cages of 11, 34, and 55 Å, the corresponding Ar adsorption isotherms at 87 K displayed the expected concave shape at low relative pressures.[36] The highly unusual adsorption behavior of Fe-**red**-MOF-1 could be associated with framework flexibility in this ultraporous material. A strong indication supporting this plausible proposition comes from scanning electron microscopy images (SEM) of activated Fe-**red**-MOF-1 cubic crystals. As shown in Figure 2d, the faces of the cubes are curved inward, making this a concave polyhedron, while the crystals maintain their integrity with sharp edges (Figure S11). Therefore, it is entirely possible that in the activated material initially the pores are shrunk to an extent and progressively open as adsorption occurs. This behavior could explain the observed convex isotherm shape in the low-pressure region, and we are currently designing important experiments to shed light on the observed phenomenon.

It is evident that Fe-**red**-MOF-1 is a hierarchically porous material with ultrahigh porosity, which to an extent could explain the weak SCXRD and PXRD diffraction using in-house instruments and the fact that most of the diffracted intensity is funneled through the low angle Bragg peaks (<10 deg 2theta). Notably, attempts to collect SCXRD diffraction data on the activated Fe-**red**-MOF-1, using synchrotron facilities as well as state-of-the-art electron diffractometers were unsuccessful. Furthermore, we collected high resolution PXRD (HR-PXRD) data using synchrotron radiation resulting in an identical pattern as compared to that obtained with an in-house instrument (Figure 2c). Notably, in the high resolution PXRD pattern sharp Bragg reflections are observed up to approximately 1.2 $Å^{-1}$ (d-spacing, 5.2 Å) followed by a diffuse scattering, indicating the absence of long-range periodicity in activated Fe-**red**-MOF-1. These results are quite surprising and could be related to the concave nature of the cubic particles observed by SEM imaging (Figure 2d). In other words, the absence of long-range periodicity in activated Fe-**red**-MOF-1 is associated with the curved faces of the cubic particles that place the atoms in noncrystallographic positions. This inherent nonperiodic arrangement of atoms in activated Fe-**red**-MOF-1 prohibits its direct structural determination by SCXRD using synchrotron radiation or dedicated electron diffraction instruments. Therefore, we looked at the RCSR database as well as in the literature to find candidate structures in which trinuclear $[Fe_3(\mu_3\text{-}O)(-COO)_6]$ cluster can be combined with the 4-c H_4TCEPT linker to afford a cubic structure with a hierarchical pore network.[37]

We hypothesized that Fe-**red**-MOF-1 is based on $[Fe_3(\mu_3\text{-}O)(-COO)_6]^+$ MBBs because these clusters are easily formed under the applied solvothermal reaction conditions. A candidate (4, 6)-c network with large mesopores could be that with the **stp-a** topology and for this reason was constructed in silico, denoted as Fe-**stp**-TCEPT (Figure S23). However, Fe-**stp**-TCEPT is based on a hexagonal rather than a cubic system and features large 1D mesopores (40 Å), lacking a hierarchical pore network. Furthermore, the calculated PXRD pattern of Fe-**stp**-TCEPT is very different compared to the experimental pattern of activated Fe-**red**-MOF-1 (Figure S37). For these reasons the **stp-a** type structure is excluded. The next candidate structure that was identified, relying also on 4-c linkers and 6-c trimers, is the computationally constructed hypo-**red**-MOF based on the **red-a** net.[10] In hypo-**red**-MOF the tetra-biphenyl carboxylate porphyrin was used as an ideal 4-c square linker with planar carboxylate arms to decorate the faces of the cubic cages (Figure 1c). Notably, it was proposed that hypo-**red**-MOF can potentially be synthesized using rectangular ligands as these are also suitable for the construction of cubic cages, observed in **soc-a** MOFs. Accordingly, based on the structural information on **red-a** net provided by the RCSR database and using the $[Fe_3(\mu_3\text{-}O)(-COO)_6]^+$ and $[TCEPT]^{4-}$ as 6-c and 4-c nodes, we successfully constructed and optimized the corresponding crystallographic file (Figure 1d,e). Importantly, during optimization, the unit cell parameter of the cubic lattice was fixed to the experimental value of 52.24 Å. Careful inspection of the optimized structure did not reveal unusual bond lengths and angles or ligand deformation. In other words, the 6-c trimer combined with the 4-c TCEPT linker fits very well into the structure based on the **red-a** net. Interestingly, this is not the case for hypo-**red**-MOF where a significant deformation of the porphyrin ligand is observed in two opposite faces of the cuboidal cages (Figure S24). However, as we explain in detail below this is not an optimization problem in hypo-**red**-MOF but originates from the fact that a 4-c square ligand cannot fit into a **red-a** net due to connectivity constraints implied by this topology.

The calculated PXRD pattern from the constructed **red-a** structure matches perfectly with the experimental pattern of Fe-**red**-MOF-1 (Figure S38). Moreover, the experimental PXRD pattern was successfully fitted using a full-profile Le Bail refinement in the space group $Pm\text{-}3m$ (Figure 2a). The refined lattice parameters, a = 52.311(10) Å, agree very well with the corresponding value determined from SCXRD data, confirming phase purity. The weighted profile R-factor (Rwp = 4.28%) indicates an excellent match between calculated and observed

https://doi.org/10.1021/jacs.5c16581
J. Am. Chem. Soc. XXXX, XXX, XXX−XXX

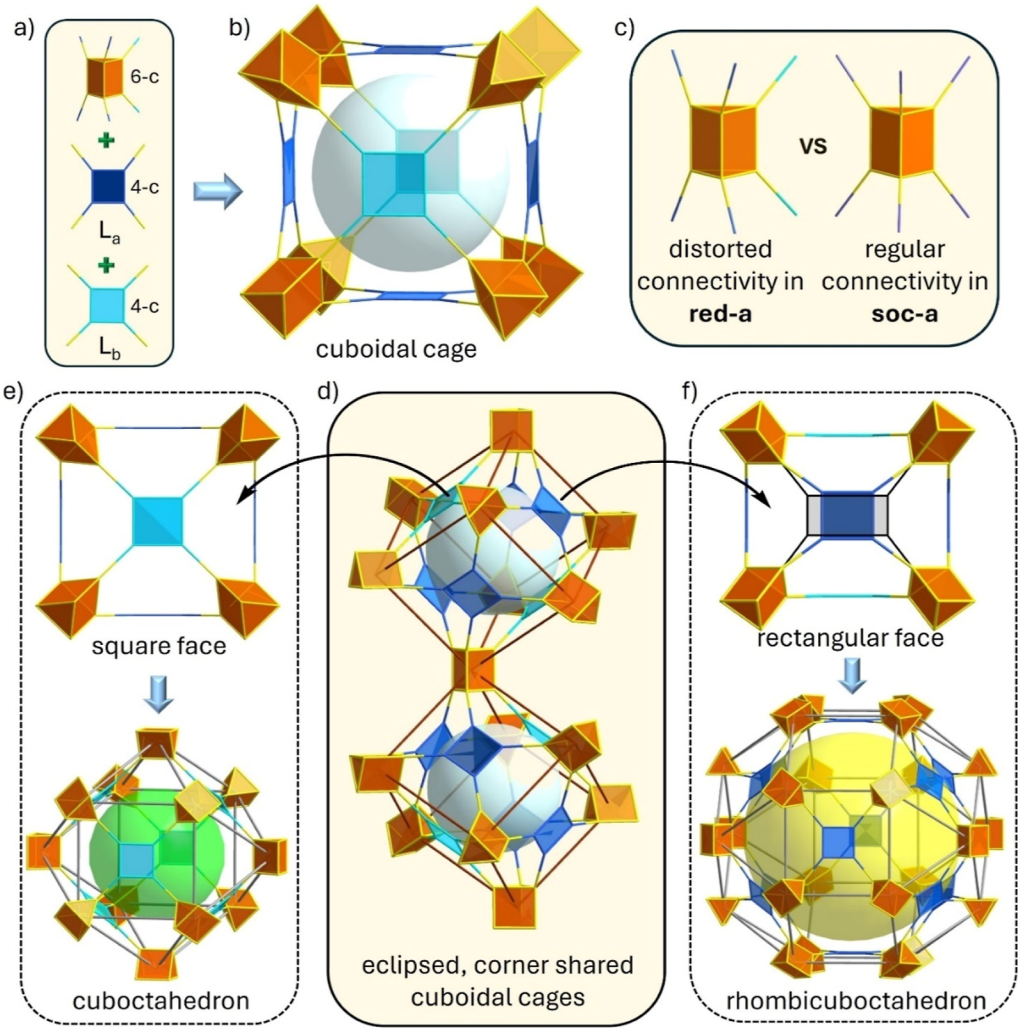

Figure 3. Augmented (4, 4, 6)-c **red-a** net constructed from the data provided in the RCSR database. (a) The distinct nodes that construct the **red-a** net. (b) The cuboidal cage in **red-a** net. (c) The distorted 6-c node in **red-a** net as compared with the regular 6-c node in **soc-a**. (d) The corner-shared cuboidal cages in **red-a** are arranged in an eclipsed conformation. Note the square (light blue) and rectangular faces (dark blue) of the cuboidal cages. The corresponding distinct 4-c nodes form distinct polyhedral cages. In particular, the 4-c node that forms square faces, forms explicitly the cuboctahedral cages in **red-a** (green sphere) (e), while the 4-c node in the rectangular faces, forms the large rhombicuboctahedral cages (yellow sphere) (f). Note in (f) that the four points of extension from the four 6-c nodes occupying the corners do not align with the face diagonals and therefore match with a 4-c rectangular node (black shape).

patterns, with no extra reflections detected. Furthermore, transmission electron microscopy images revealed the presence of a square-like periodicity of approximately 40 Å, as expected from the primitive cubic arrangement of the large mesopores in the crystal structure based on the **red-a** net (Figures 2b and S18). Notably, the observed TEM periodicity length is smaller than the expected mesopore-to-mesopore distance in the ideal cubic structure which is equal to the unit cell edge of 52.31 Å.

Considering that the cubic faces, along which the square mesopore periodicity is observed (Figure 1e), are not flat but curved inward (Figure 2d), their 2D projection in the TEM images will cause the mesopore-to-mesopore distance to appear smaller. The combined important experimental results from SCXRD, PXRD, SEM, TEM and Ar sorption isotherm coupled with in-silico materials construction, leave no doubts that Fe-**red**-MOF-1 displays the awaited **red-a** topology. Table S4 summarizes the experimental and calculated data derived from the in-silico constructed MOF structures, based on which the **red-a** topology matches perfectly with Fe-**red**-MOF-1, while both **soc-a** and **stp-a** are excluded.

At this point it is important to address the fundamental question, why the H_4TCEPT linker promotes the formation of the **red-a** net instead of the **soc-a** net. To answer this question, we need to look carefully at the ideal **red-a** structure provided in the RCSR database and, in particular, at the different polyhedral cages that exist in this unique 3D network. As shown in Figure 3a,b, a cuboidal cage is formed by two crystallographically distinct, face decorating 4-c square nodes (L_a: dark blue L_b: light blue) that link 6-c trigonal prismatic nodes and this is the reason why **red-a** is a (4, 4, 6)-c network and not a (4, 6)-c net as the **soc-a**. Each cage accommodates two L_b nodes decorating opposite faces and four L_a nodes (Figure 3b). Notably, the two L_b decorated faces are perfect squares (Figure 3e) while those based on L_a nodes are in fact rectangular faces (Figure 3f). This is because in a L_a decorated face, the four points of extension from the four 6-c nodes occupying the corners do not align with the face diagonals and therefore match with a 4-c rectangular node (black shape in Figure 3f), rather than a 4-c square node. In other words, a 4-c square node needs to become distorted to decorate this face.

https://doi.org/10.1021/jacs.5c16581
J. Am. Chem. Soc. XXXX, XXX, XXX−XXX

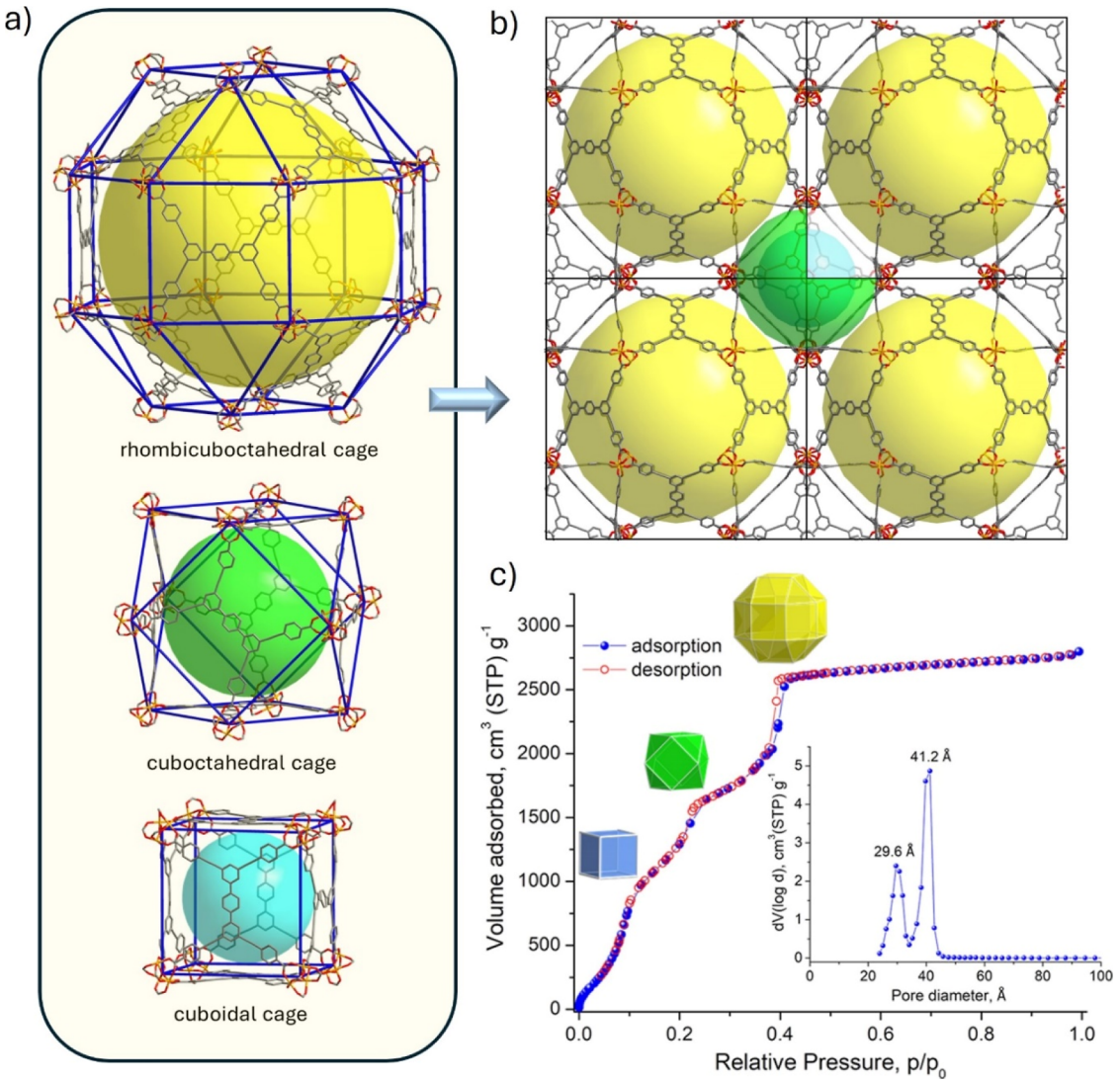

Figure 4. (a) The distinct polyhedral cages with hierarchical porosity in Fe-**red**-MOF-1. (b) View along the *c*-axis, highlighting the primitive packing of the large, face-shared mesoporous cages (yellow spheres) in Fe-**red**-MOF-1. The smaller cuboctahedral and cuboidal cages are located at the center, in an alternating arrangement. (c) Argon sorption isotherm of $scCO_2$ activated Fe-**red**-MOF-1 recorded at 87 K, displaying three distinct steps associated with the three different polyhedral cages of the **red-a** net. Inset shows the PSD curve obtained by fitting the isotherm in the range 0.1−0.99 p/p_0 with an appropriate NLDFT kernel.

Therefore, the ideal cuboidal cage in **red-a** consists of two square (L_b) and four rectangular faces (L_a) (Figure 3b) and each 6-c trigonal prismatic node is in fact a distorted node, connected to four L_a and two L_b, in contrast to the regular connectivity observed in **soc-a** or **edq-a** nets (Figure 3c).[27,38] This distortion originates from the fact that the corner-shared cuboidal cages in **red-a** net are in an eclipsed conformation, in contrast to the staggered corner-shared cubes in **soc-a** or **edq-a** nets (Figures 3d, S25 and S26). This is also evident in the simplified parent **reo-e** net, where the corner-shared cubes are rotated by 60° relative to each other (eclipsed form). (Figure 1a).[10] Therefore, the ideal **red-a** net inherently requires two geometrically distinct 4-c linkers, one square and one rectangular, to match the points of extension of the 6-c trigonal prismatic nodes, thereby forming face-decorated, corner-shared cuboidal cages in an eclipsed form. Interestingly, in **red-a** the cuboctahedral and rhombicuboctahedral cages are formed exclusively by L_b and L_a 4-c nodes, respectively (Figure 3e,f).

For a given 4-c carboxylate-based organic linker, the geometric requirements to fit into a **red-a** net, when combined with 6-c trigonal prismatic M_3O clusters, is to exhibit square (or near-square) metrics—measured between the carbon atoms of the carboxylate groups—while maintaining a rectangular linking topology (Figure S27a). In that case, minimum linker distortions are expected to form both the square and the rectangular faces of the cuboidal cages. At the same time, this kind of 4-c linker is not suitable to form the **soc-a** net, as in this case a rectangular shape, rather than a square, is required (Figure S25a). This is exactly the case for the H_4TCEPT linker, which has a nearly square shape with a rectangular linking topology (Figure S27b). As expected, the cuboidal cages in Fe-**red**-MOF-1 consist of two crystallographically distinct TCEPT linkers, denoted as TCEPT-a and TCEPT-b, decorating rectangular and square faces respectively, with minimum distortions (Figure S27c,d). Considering the absence of Cl^- anions as confirmed by EDS analysis (Figure S8), the overall charge balanced chemical formula of

https://doi.org/10.1021/jacs.5c16581
J. Am. Chem. Soc. XXXX, XXX, XXX−XXX

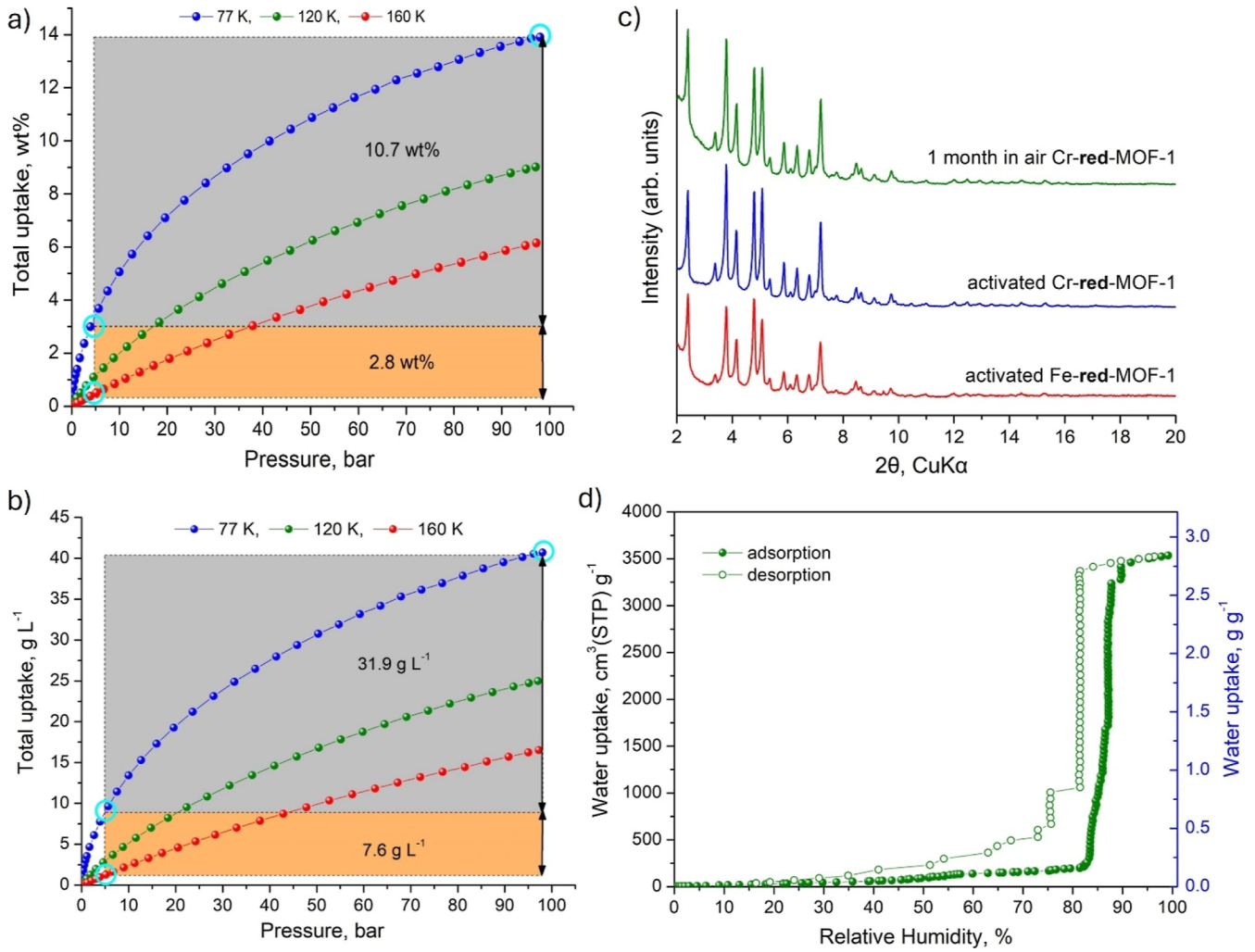

Figure 5. Hydrogen sorption isotherms of Fe-**red**-MOF-1 at cryogenic conditions, indicating the corresponding (a) gravimetric and (b) volumetric working capacities, under isothermal pressure swing (gray area) and pressure−temperature swing (gray and orange area). (b) PXRD pattern of freshly $scCO_2$ activated Cr-**red**-MOF-1 (blue line) and after 1 month exposed to air (green line). For comparison, the PXRD pattern of activated Fe-**red**-MOF-1 (red line) is also shown. (d) Water sorption isotherm of Cr-**red**-MOF-1 recorded at 298 K.

Fe-**red**-MOF-1 is $(Fe_3O)_2(TCEPT\text{-}a)_2(TCEPT\text{-}b)(OH)_2(H_2O)_4$. This formula is confirmed by thermogravimetric analysis (TGA) of activated Fe-**red**-MOF-1, recorded under air flow. Accordingly, the TGA trace shows a major weight loss between 300 and 400 °C, corresponding to 82.2%, which is very close to the expected value of 83.4% based on the chemical formula, considering the formation of a-Fe_2O_3 as confirmed by the PXRD analysis of the remaining red solid after the TGA experiment (Figure S59a,c). The stability of Fe-**red**-MOF-1 in various organic solvents was evaluated and the material was found to be stable in ethanol, methanol, acetonitrile and dichloromethane as revealed by PXRD measurements (Figure S41).

The distinct polyhedral cages formed by the 3D packing of the corner-shared cuboidal cages in Fe-**red**-MOF-1 are shown in Figure 4a,b. Geometric analysis using the Zeo++ software revealed a largest cavity diameter of 43.2 Å (Table S1), which is very close to the mesoporous size of 41.2 Å obtained from the Ar adsorption isotherm of Fe-**red**-MOF-1 (Figure 4c).[39] The remarkable hierarchical porosity of Fe-**red**-MOF-1 is considered very important for gas storage applications and in particular for hydrogen.[40] Accordingly, we investigated in detail the corresponding H_2 storage properties at cryogenic conditions and high pressures, which are relevant for real-world applications, with highly promising results, as we describe below. High-pressure adsorption experiments were conducted volumetrically at 77, 120 and 160 K on $scCO_2$ activated Fe-**red**-MOF-1. For these measurements, special attention has been given to volume calibrations, which were carried out in a way to completely avoid errors related to helium adsorption. The corresponding adsorption isotherms are presented in Figure 5a,b. It is noted that although the actual experimentally measured quantity is always the Gibbsian surface excess, the results are presented as total amounts adsorbed since this approach is more relevant for gas storage applications. Notably the total H_2 uptake at 77 K upon charging with 100 bar is 13.9 wt % (161.5 mg H_2 per g of MOF), while the working capacities for isothermal pressure swing (100 to 5 bar at 77 K) and pressure−temperature swing (77 K-100 bar to 160 K-5 bar) are calculated to be 10.7 and 13.5 wt %, respectively (Figure 5a). Taking into account the bulk density of Fe-**red**-MOF-1, the latter corresponds to a working volumetric capacity of 39.5 g L^{-1} (Figure 5b) These well balanced high gravimetric and volumetric deliverable capacities, place Fe-**red**-MOF-1 in the list of top performing materials for cryo-adsorptive hydrogen storage, including NU-

https://doi.org/10.1021/jacs.5c16581
J. Am. Chem. Soc. XXXX, XXX, XXX−XXX

1501-Al (14 wt %/46.2 g L^{-1}), NU-100/PCN-610 (13.9 wt %/47.6 g L^{-1}), Fe-**tbb**-MOF-2 (11.6 wt %/41.4 g L^{-1}), SNU-70 (10.6 wt %/47.9 g L^{-1}) and NOT-112 (9.1 wt %/41 g L^{-1}) (see Table S6 and Figure S57).[40] The H_2 isosteric heat of adsorption (Q_{st}) was calculated as a function of coverage by simultaneous fitting of the adsorption isotherms by the virial equation revealing a relatively weak H_2-MOF interaction (2−4 kJ mol^{-1}), which is moreover decreasing upon loading, as expected (Figures S55 and S56). It should be emphasized that such low heats of adsorption are highly desirable for cryogenic hydrogen storage, for two main reasons: (a) they minimize the amount of hydrogen retained at the release pressure (5 bar), and (b) they reduce temperature fluctuations during adsorption/desorption, thereby simplifying heat management at the storage tank level.

The discovery of Fe-**red**-MOF-1 provides great opportunities to access isostructural MOFs through postsynthetic metal-exchange strategies.[33,41−44] Accordingly, we successfully synthesized Cr-**red**-MOF-1 by reacting Fe-**red**-MOF-1 with $CrCl_2$ in DMF under inert conditions. A facile topotactic exchange reaction of Fe^{3+} by Cr^{3+} is due to favorable redox thermodynamics, coupled with ligand field stabilization energy (LFSE) effects and M−O bond strength following the Hard−soft acid−base (HSAB) principle.[42,44] Accordingly, the M^{3+}/M^{2+} redox potentials for Fe and Cr (+0.77 V for Fe and −0.42 V for Cr in aqueous solutions) strongly favors the reduction of Fe^{3+} within the Fe_3O-trimer by Cr^{2+} which is oxidized to Cr^{3+}. This results in the formation of labile Fe^{2+} which is replaced by Cr^{3+} because the latter has higher LFSE and in addition, forms stronger M-O bonds due to its smaller ionic radius (octahedral, 0.615 Å) as compared to Fe^{3+} (octahedral 0.645 Å) making it a harder Lewis acid. The presence of Cr^{3+} in Cr-**red**-MOF-1 was confirmed by XPS. Accordingly, the Cr 2p XPS spectrum containing two main peaks centered at 576.72 and 586.24 eV, corresponding to Cr $^{3+}(2p_{3/2})$ and $Cr^{3+}(2p_{1/2})$ respectively, in full agreement with literature data (Figure S60).[45]

Complete metal exchange was confirmed by EDS spectroscopy and SEM images demonstrate the Cr-**red**-MOF-1 maintains the crystallinity and the cuboidal particle shape of the parent Fe-**red**-MOF-1 (Figures S9 and S10). In this case the $[Cr_3(\mu_3\text{-}O)(-COO)_6]^+$ trimers are charge balanced by Cl^- anions (Figure S10). Thermogravimetric analysis is consistent with the chemical formula of $(Cr_3O)_2$(TCEPT-a)$_2$(TCEPT-b)$(Cl)_2(H_2O)_4$ (Figure S59b). Cr-**red**-MOF-1 is found stable in common organic solvents and water, as confirmed by PXRD measurements (Figure S42).

The in-house PXRD pattern of $scCO_2$ activated Cr-**red**-MOF-1 is identical to that of Fe-**red**-MOF-1 demonstrating that both MOFs are isostructural compounds (Figure 5c). This is also confirmed by HR-PXRD data recorded at synchrotron facilities (Figures S39 and S40). The porosity of Cr-**red**-MOF-1 was confirmed by Ar sorption at 87 K where a multistep isotherm, almost identical to that of Fe-**red**-MOF-1 is recorded with a slightly lower total pore volume of 3.39 $cm^3\ g^{-1}$ and a BET surface area of 5190 $m^2\ g^{-1}$ (Figures S46 and S49). Notably, after one month exposure in air the $scCO_2$ activated Cr-**red**-MOF-1 shows no reduction in crystallinity as confirmed by PXRD (Figure 5c). The enhanced hydrolytic stability of Cr-**red**-MOF-1 coupled with its ultrahigh hierarchical porosity, prompted us to investigate the water sorption property at room temperature. Accordingly, using a state-of-the-art volumetric vapor sorption instrument, a water isotherm was recorded at 298 K up to saturation, revealing an S-type curve with a sharp adsorption step between 80−90% RH, followed by a plateau (Figure 5d). Remarkably, the water uptake at 95% RH reaches 3500 cm^3 (STP) g^{-1}, corresponding to an exceptional capacity of 281 wt % (2.81 g g^{-1}). To the best of our knowledge, this remarkable uptake substantially exceeds that of the top-performing MOFs, including Cr-**soc**-MOF-1 (195 wt %) and Cr-Spiro-5 (176 wt %) (Table S7 and Figure S58).[33,46,47] The calculated total pore volume from the water isotherm at 99% RH is 2.85 $cm^3\ g^{-1}$ which is close to the corresponding value obtained from the Argon isotherm at 87 K. The desorption curve shows a small gradual decrease in uptake with a relatively narrow hysteresis up to 81% RH where a remarkably steep step is observed, approximating a straight line, down to 1000 $cm^3\ g^{-1}$, indicating an unrestricted water vapor release (71%) up to this point (Figure 5d). This extremely steep desorption step is followed by a gradual, multistep water vapor release down to low RH levels, where the adsorption and desorption branches coincide. Notably, the PXRD of the Cr-**red**-MOF-1 after this complete water adsorption−desorption cycle, shows only a broad Bragg peak at low diffraction angles, followed by diffuse scattering, indicating loss of periodicity (Figure S44). Considering that the activated Cr-**red**-MOF-1 maintains its crystallinity upon exposure to air for at least a month (Figure 5c), the observed loss of crystallinity after a single water adsorption−desorption cycle is attributed to the strong capillary forces during water desorption in combination with the plausible flexible nature of the framework, described previously. We are currently investigating in detail the associated water sorption mechanism and in addition, we explore reticular chemistry approaches to stabilize the Cr-**red**-MOF-1 framework.

Finally, to demonstrate the generalization of the proposed design strategy that a *4-c organic linker with nearly square metrics and rectangular connectivity* leads to MOFs with **red-a** topology, we have successfully synthesized and characterized new isoreticular members, denoted as M-**red**-MOF-2 (M = Fe, Cr), based on the anthracene derived analogue 4,4′,4″,4‴-((anthracene-9,10-diylbis(benzene-5,1,3-triyl))tetrakis(ethyne-2,1-diyl))tetrabenzoic acid, denoted as H_4TEBDA (Figure S28). This is confirmed by SCXRD measurements for unit cell determination (Figures S31, S32 and Table S2), PXRD (Figure S43), SEM imaging (Figure S12) and Ar sorption measurements at 87 K where the expected hierarchical porosity is confirmed (Figure S51 and Table S5). Notably, in these cases, the convex shape of the first adsorption step is less pronounced compared to M-**red**-MOF-1, and a very good NLDFT fit was obtained, revealing all three pore sizes, 16.2, 28.5, and 38.2 Å, of the hierarchical cages (Figure S53). This may reflect a reduced linker flexibility associated with the anthracene core. Interestingly, SEM images of activated M-**red**-MOF-2 show less curved faces of the cubic crystals. We are currently investigating in detail this behavior.

Further proof that the proposed design strategy for the reticular synthesis of **red-a** MOFs is valid comes from a very recent report in ChemRxiv, where the authors used the linker 4,4′,4″,4‴-((ethyne-1,2-diylbis(benzene-5,1,3-triyl))tetrakis-(ethyne-2,1-diyl))tetrabenzoic acid and synthesized CU-6-M (M = Fe or Cr) displaying the **red-a** topology.[48] In this case, the linker has a diphenylethyne core (−Ph−C≡C−Ph−) instead of a terphenyl (−Ph−Ph−Ph−) in Fe-**red**-MOF-1, and therefore is slightly shorter, making this an almost perfect square while maintaining the rectangular connectivity (Figure S28).

https://doi.org/10.1021/jacs.5c16581
J. Am. Chem. Soc. XXXX, XXX, XXX−XXX

CONCLUSIONS

This work demonstrates that it is possible to construct novel ultraporous MOFs, denoted as M-**red**-MOF-x (x = 1, 2; M = Fe, Cr), displaying the awaited **red-a** topology using suitable 4-c organic linkers combined with 6-c trigonal prismatic $[M_3(\mu_3\text{-}O)(-COO)_6]^+$ (M: Fe^{3+}, Cr^{3+}) SBBs. In particular, the use of H_4TCEPT as a 4-c linker having a nearly square shape but a rectangular connectivity (opposite carboxylate groups are not aligned diagonally) match the geometric requirements of the **red-a** net and readily afforded Fe-**red**-MOF-1 when reacted solvothermally with $FeCl_3{\cdot}6H_2O$. Extensive structural characterization using SCXRD for unit cell determination, PXRD, SEM, TEM imaging and detailed gas sorption isotherms, coupled with in-silico materials construction, confirmed that Fe-**red**-MOF-1 display the **red-a** topology. The material displays a unique hierarchical pore system with an ultrahigh total pore volume of 3.56 $cm^3\ g^{-1}$ originating from the combination of face share cuboidal, cuboctahedral (29.6 Å) and rhombicuboctahedral (41.2 Å) cages, as revealed by detailed Argon sorption measurements at 87 K. Interestingly, the single cuboidal particles of activated Fe-**red**-MOF-1 exhibit highly curved faces (convex polyhedra), indicative of structural flexibility. This observation is further supported by the Ar sorption isotherm and explains the lack of atomic periodicity. The hierarchical ultrahigh porosity of Fe-**red**-MOF-1 is very well suited for important gas storage applications. Accordingly, hydrogen sorption measurement under cryogenic conditions place Fe-**red**-MOF-1 among the top performing MOFs, demonstrating an exceptional gravimetric deliverable capacity of 13.5 wt %. The isostructural Cr-**red**-MOF-1 was successfully synthesized by postsynthetic metal exchange reaction. The water sorption properties of this material were studied by recording the corresponding isotherm at 298 K up to saturation, revealing an astonishing uptake of 2.81 $g\ g^{-1}$, which is significantly larger than that of the current top-ranking MOF, Cr-**soc**-MOF-1 (1.95 $g\ g^{-1}$). Finally, we validated the proposed design strategy namely, that a 4-connected organic linker with nearly square metrics and rectangular connectivity leads to MOFs with the **red-a** topology, through the reticular synthesis of the new members M-**red**-MOF-2 (M = Fe, Cr), based on the anthracene-derived analogue H_4TEBDA.

The successful synthesis of M-**red**-MOF-x (x = 1, 2; M = Fe, Cr) provides key design principles for the reticular synthesis of novel materials with the unique **red-a** topology, thereby facilitating the expansion of this important family of MOFs. The reticular design and construction of MOFs with a hierarchical pore system associated with the **red-a** net open new opportunities for the development of tailor-made porous materials for advanced applications. Their well-defined pore networks and tunable frameworks could be leveraged in catalysis for selective chemical transformations, in energy storage systems such as batteries or supercapacitors, as carriers for controlled drug delivery, and in photonic or sensing devices where precise framework architecture is critical. These prospects highlight the potential of MOFs with **red-a** topology to serve as multifunctional platforms for next-generation technologies.

ASSOCIATED CONTENT

Supporting Information

The Supporting Information is available free of charge at https://pubs.acs.org/doi/10.1021/jacs.5c16581.

Experimental details, single-crystal and powder XRD data, SEM and TEM images, additional gas sorption isotherms, NMR, TGA and XPS analysis (PDF)

Accession Codes

Deposition Numbers 2483752−2483754 contain the supplementary crystallographic data for this paper. These data can be obtained free of charge via the joint Cambridge Crystallographic Data Centre (CCDC) and Fachinformationszentrum Karlsruhe Access Structures service.

AUTHOR INFORMATION

Corresponding Author

Pantelis N. Trikalitis − *Department of Chemistry, University of Crete, Heraklion 71003, Greece;* orcid.org/0000-0002-6286-2955; Email: ptrikal@uoc.gr

Authors

Konstantinos G. Froudas − *Department of Chemistry, University of Crete, Heraklion 71003, Greece*

Constantinos Tsangarakis − *Department of Chemistry, University of Crete, Heraklion 71003, Greece*

Tamsyn Montagnon − *Department of Chemistry, University of Crete, Heraklion 71003, Greece;* orcid.org/0009-0005-5678-4013

Charalampos Livas − *Department of Chemistry, University of Crete, Heraklion 71003, Greece*

Emmanuel Klontzas − *Theoretical and Physical Chemistry Institute, National Hellenic Research Foundation, GR-116 35 Athens, Greece;* orcid.org/0000-0002-1974-5198

George E. Froudakis − *Department of Chemistry, University of Crete, Heraklion 71003, Greece;* orcid.org/0000-0002-6907-1822

Christos Tampaxis − *National Center for Scientific Research "Demokritos", Athens 15341, Greece*

Georgia Charalambopoulou − *National Center for Scientific Research "Demokritos", Athens 15341, Greece*

Theodore A. Steriotis − *National Center for Scientific Research "Demokritos", Athens 15341, Greece*

Complete contact information is available at: https://pubs.acs.org/10.1021/jacs.5c16581

Funding

The open access publishing of this article is financially supported by HEAL-Link.

Notes

The authors declare no competing financial interest.

ACKNOWLEDGMENTS

Authors acknowledge financial support from European Union: Horizon Europe (project MOST-H2; Grant agreement no. 101058547). We acknowledge the European Synchrotron Radiation Facility (ESRF) for provision of synchrotron radiation facilities and Momentum Transfer for facilitating the measurements. Jakub Drnec is thanked for assistance and support in using beamline ID31. The measurement setup was developed with funding from the European Union's Horizon 2020 research and innovation program under the STREAMLINE project (grant agreement ID 870313). Measurements performed as part of the MatScatNet project were supported by OSCARS through the European Commission's Horizon Europe Research and Innovation programme under grant agreement No. 101129751.

REFERENCES

(1) Furukawa, H.; Cordova, K. E.; O'Keeffe, M.; Yaghi, O. M. The Chemistry and Applications of Metal-Organic Frameworks. *Science* **2013**, *341* (6149), 1230444.

(2) Jiang, H.; Alezi, D.; Eddaoudi, M. A reticular chemistry guide for the design of periodic solids. *Nat. Rev. Mater.* **2021**, *6* (6), 466−487.

(3) Kaskel, S. The Chemistry of Metal−Organic Frameworks. In *Synthesis, Characterization, and Applications*; Wiley, 2016.

(4) Freund, R.; Canossa, S.; Cohen, S. M.; Yan, W.; Deng, H.; Guillerm, V.; Eddaoudi, M.; Madden, D. G.; Fairen-Jimenez, D.; Lyu, H.; Macreadie, L. K.; Ji, Z.; Zhang, Y.; Wang, B.; Haase, F.; Wöll, C.; Zaremba, O.; Andreo, J.; Wuttke, S.; Diercks, C. S. 25 Years of Reticular Chemistry. *Angew. Chem., Int. Ed.* **2021**, *60* (45), 23946−23974.

(5) Yaghi, O. M.; Kalmutzki, M. J.; Diercks, C. S. *Introduction to Reticular Chemistry*; Wiley, 2019.

(6) Chen, Z.; Kirlikovali, K. O.; Li, P.; Farha, O. K. Reticular Chemistry for Highly Porous Metal−Organic Frameworks: The Chemistry and Applications. *Acc. Chem. Res.* **2022**, *55* (4), 579−591.

(7) O'Keeffe, M.; Yaghi, O. M. Deconstructing the Crystal Structures of Metal−Organic Frameworks and Related Materials into Their Underlying Nets. *Chem. Rev.* **2012**, *112* (2), 675−702.

(8) Jiang, H.; Benzaria, S.; Alsadun, N.; Jia, J.; Czaban-Jóźwiak, J.; Guillerm, V.; Shkurenko, A.; Thiam, Z.; Bonneau, M.; Maka, V. K.; Chen, Z.; Ameur, Z. O.; O'Keeffe, M.; Eddaoudi, M. Merged-nets enumeration for the systematic design of multicomponent reticular structures. *Science* **2024**, *386* (6722), 659−666.

(9) Chen, Z.; Jiang, H.; Li, M.; O'Keeffe, M.; Eddaoudi, M. Reticular Chemistry 3.2: Typical Minimal Edge-Transitive Derived and Related Nets for the Design and Synthesis of Metal−Organic Frameworks. *Chem. Rev.* **2020**, *120* (16), 8039−8065.

(10) Guillerm, V.; Eddaoudi, M. Material Design and Reticular Chemistry: Unveiling New Topologies through Face Decoration of Edge Nets. *nd. Eng. Chem. Res.* **2022**, *61* (34), 12641−12648.

(11) Wilmer, C. E.; Leaf, M.; Lee, C. Y.; Farha, O. K.; Hauser, B. G.; Hupp, J. T.; Snurr, R. Q. Large-scale screening of hypothetical metal−organic frameworks. *Nat. Chem.* **2012**, *4* (2), 83−89.

(12) Bobbitt, N. S.; Chen, J.; Snurr, R. Q. High-Throughput Screening of Metal−Organic Frameworks for Hydrogen Storage at Cryogenic Temperature. *J. Phys. Chem. C* **2016**, *120* (48), 27328−27341.

(13) Chen, Z.; Thiam, Z.; Shkurenko, A.; Weselinski, L. J.; Adil, K.; Jiang, H.; Alezi, D.; Assen, A. H.; O'Keeffe, M.; Eddaoudi, M. Enriching the Reticular Chemistry Repertoire with Minimal Edge-Transitive Related Nets: Access to Highly Coordinated Metal−Organic Frameworks Based on Double Six-Membered Rings as Net-Coded Building Units. *J. Am. Chem. Soc.* **2019**, *141* (51), 20480−20489.

(14) Guillerm, V.; Maspoch, D. Geometry Mismatch and Reticular Chemistry: Strategies To Assemble Metal−Organic Frameworks with Non-default Topologies. *J. Am. Chem. Soc.* **2019**, *141* (42), 16517−16538.

(15) Li, P.; Vermeulen, N. A.; Malliakas, C. D.; Gómez-Gualdrón, D. A.; Howarth, A. J.; Mehdi, B. L.; Dohnalkova, A.; Browning, N. D.; O'Keeffe, M.; Farha, O. K. Bottom-up construction of a superstructure in a porous uranium-organic crystal. *Science* **2017**, *356* (6338), 624−627.

(16) Lee, S.; Lee, S.; Kwak, Y.; Yousaf, M.; Cho, E.; Moon, H. R.; Cho, S. J.; Park, N.; Choe, W. Parsimonious Topology Based on Frank-Kasper Polyhedra in Metal−Organic Frameworks. *JACS Au* **2024**, *4* (7), 2539−2546.

(17) Alsadun, N.; Mouchaham, G.; Guillerm, V.; Czaban-Jóźwiak, J.; Shkurenko, A.; Jiang, H.; Bhatt, P. M.; Parvatkar, P.; Eddaoudi, M. Introducing a Cantellation Strategy for the Design of Mesoporous Zeolite-like Metal−Organic Frameworks: Zr-sod-ZMOFs as a Case Study. *J. Am. Chem. Soc.* **2020**, *142* (49), 20547−20553.

(18) Alezi, D.; Spanopoulos, I.; Tsangarakis, C.; Shkurenko, A.; Adil, K.; Belmabkhout, Y.; O'Keeffe, M.; Eddaoudi, M.; Trikalitis, P. N. Reticular Chemistry at Its Best: Directed Assembly of Hexagonal Building Units into the Awaited Metal-Organic Framework with the Intricate Polybenzene Topology, pbz-MOF. *J. Am. Chem. Soc.* **2016**, *138* (39), 12767−12770.

(19) Férey, G.; Serre, C.; Mellot-Draznieks, C.; Millange, F.; Surblé, S.; Dutour, J.; Margiolaki, I. A Hybrid Solid with Giant Pores Prepared by a Combination of Targeted Chemistry, Simulation, and Powder Diffraction. *Angew. Chem., Int. Ed.* **2004**, *43* (46), 6296−6301.

(20) Mellot-Draznieks, C.; Dutour, J.; Férey, G. Computational Design of Hybrid Frameworks: Structure and Energetics of Two Me3OF3{-O2C-C6H4-CO2-}3 Metal-Dicarboxylate Polymorphs, MIL-hypo-1 and MIL-hypo-2. *Z. Anorg. Allg. Chem.* **2004**, *630* (15), 2599−2604.

(21) Férey, G.; Mellot-Draznieks, C.; Serre, C.; Millange, F.; Dutour, J.; Surblé, S.; Margiolaki, I. A Chromium Terephthalate-Based Solid with Unusually Large Pore Volumes and Surface Area. *Science* **2005**, *309* (5743), 2040−2042.

(22) O'Keeffe, M.; Hyde, B. G. *Crystal Structures I. Patterns and Symmetry* (Chapter 6, p 276), Mineralogical Society of America, WA, DC 1996.

(23) Wei, Y.-S.; Shen, J.-Q.; Liao, P.-Q.; Xue, W.; Zhang, J.-P.; Chen, X.-M. Synthesis and stabilization of a hypothetical porous framework based on a classic flexible metal carboxylate cluster. *Dalton Trans.* **2016**, *45* (10), 4269−4273.

(24) Ren, G.; Liu, S.; Wei, F.; Ma, F.; Tang, Q.; Li, S. A polyhedron-based metal−organic framework with a reo-e net. *Dalton Trans.* **2012**, *41* (38), 11562−11564.

(25) Schoedel, A.; Zaworotko, M. J. [M3(μ3-O)(O2CR)6] and related trigonal prisms: versatile molecular building blocks for crystal engineering of metal−organic material platforms. *Chem. Sci.* **2014**, *5* (4), 1269−1282.

(26) Sudik, A. C.; Côté, A. P.; Yaghi, O. M. Metal-Organic Frameworks Based on Trigonal Prismatic Building Blocks and the New "acs" Topology. *Inorg. Chem.* **2005**, *44* (9), 2998−3000.

(27) Alezi, D.; Belmabkhout, Y.; Suyetin, M.; Bhatt, P. M.; Weseliński, Ł. J.; Solovyeva, V.; Adil, K.; Spanopoulos, I.; Trikalitis, P. N.; Emwas, A.-H.; Eddaoudi, M. MOF Crystal Chemistry Paving the Way to Gas Storage Needs: Aluminum-Based soc-MOF for CH4, O2, and CO2 Storage. *J. Am. Chem. Soc.* **2015**, *137* (41), 13308−13318.

(28) Froudas, K. G.; Vassaki, M.; Papadopoulos, K.; Tsangarakis, C.; Chen, X.; Shepard, W.; Fairen-Jimenez, D.; Tampaxis, C.; Charalambopoulou, G.; Steriotis, T. A.; Trikalitis, P. N. Expanding the Reticular Chemistry Building Block Library toward Highly Connected Nets: Ultraporous MOFs Based on 18-Connected Ternary, Trigonal Prismatic Superpolyhedra. *J. Am. Chem. Soc.* **2024**, *146* (13), 8961−8970.

(29) Krause, S.; Evans, J. D.; Bon, V.; Senkovska, I.; Iacomi, P.; Kolbe, F.; Ehrling, S.; Troschke, E.; Getzschmann, J.; Többens, D. M.; Franz, A.; Wallacher, D.; Yot, P. G.; Maurin, G.; Brunner, E.; Llewellyn, P. L.; Coudert, F.-X.; Kaskel, S. Towards general network architecture design criteria for negative gas adsorption transitions in ultraporous frameworks. *Nat. Commun.* **2019**, *10* (1), 3632.

(30) Furukawa, H.; Ko, N.; Go, Y. B.; Aratani, N.; Choi, S. B.; Choi, E.; Yazaydin, A. O.-.; Snurr, R. Q.; O'Keeffe, M.; Kim, J.; Yaghi, O. M. Ultrahigh Porosity in Metal-Organic Frameworks. *Science* **2010**, *329* (5990), 424−428.

(31) Farha, O. K.; Eryazici, I.; Jeong, N. C.; Hauser, B. G.; Wilmer, C. E.; Sarjeant, A. A.; Snurr, R. Q.; Nguyen, S. T.; Yazaydın, A. O.-.; Hupp, J. T. Metal−Organic Framework Materials with Ultrahigh Surface Areas: Is the Sky the Limit? *J. Am. Chem. Soc.* **2012**, *134* (36), 15016−15021.

(32) Hönicke, I. M.; Senkovska, I.; Bon, V.; Baburin, I. A.; Bönisch, N.; Raschke, S.; Evans, J. D.; Kaskel, S. Balancing Mechanical Stability and Ultrahigh Porosity in Crystalline Framework Materials. *Angew. Chem., Int. Ed.* **2018**, *57* (42), 13780−13783.

(33) Towsif Abtab, S. M.; Alezi, D.; Bhatt, P. M.; Shkurenko, A.; Belmabkhout, Y.; Aggarwal, H.; Weseliński, Ł. J.; Alsadun, N.; Samin, U.; Hedhili, M. N.; Eddaoudi, M. Reticular Chemistry in Action: A

https://doi.org/10.1021/jacs.5c16581
J. Am. Chem. Soc. XXXX, XXX, XXX−XXX

Hydrolytically Stable MOF Capturing Twice Its Weight in Adsorbed Water. *Chem.* **2018**, *4* (1), 94−105.
(34) Gómez-Gualdrón, D. A.; Moghadam, P. Z.; Hupp, J. T.; Farha, O. K.; Snurr, R. Q. Application of Consistency Criteria To Calculate BET Areas of Micro- And Mesoporous Metal−Organic Frameworks. *J. Am. Chem. Soc.* **2016**, *138* (1), 215−224.
(35) Lowell, S.; Shields, J. E.; Thomas, M. A.; Thommes, M. *Characterization of Porous Solids and Powders: Surface Area, Pore Size and Density*; Kluwer Academic Publishers: Dordrecht/Boston/London, 2004.
(36) Feng, D.; Liu, T.-F.; Su, J.; Bosch, M.; Wei, Z.; Wan, W.; Yuan, D.; Chen, Y.-P.; Wang, X.; Wang, K.; Lian, X.; Gu, Z.-Y.; Park, J.; Zou, X.; Zhou, H.-C. Stable metal-organic frameworks containing single-molecule traps for enzyme encapsulation. *Nat. Commun.* **2015**, *6* (1), 5979.
(37) O'Keeffe, M.; Peskov, M. A.; Ramsden, S. J.; Yaghi, O. M. The Reticular Chemistry Structure Resource (RCSR) Database of, and Symbols for, Crystal Nets. *Acc. Chem. Res.* **2008**, *41* (12), 1782−1789.
(38) Li, M.; Li, D.; O'Keeffe, M.; Yaghi, O. M. Topological Analysis of Metal−Organic Frameworks with Polytopic Linkers and/or Multiple Building Units and the Minimal Transitivity Principle. *Chem. Rev.* **2014**, *114* (2), 1343−1370.
(39) Willems, T. F.; Rycroft, C. H.; Kazi, M.; Meza, J. C.; Haranczyk, M. Algorithms and tools for high-throughput geometry-based analysis of crystalline porous materials. *Microporous Mesoporous Mater.* **2012**, *149* (1), 134−141.
(40) Chen, Z.; Kirlikovali, K. O.; Idrees, K. B.; Wasson, M. C.; Farha, O. K. Porous materials for hydrogen storage. *Chem.* **2022**, *8* (3), 693−716.
(41) Brozek, C. K.; Dincă, M. Cation exchange at the secondary building units of metal−organic frameworks. *Chem. Soc. Rev.* **2014**, *43* (16), 5456−5467.
(42) Lian, X.; Feng, D.; Chen, Y.-P.; Liu, T.-F.; Wang, X.; Zhou, H.-C. The preparation of an ultrastable mesoporous Cr(iii)-MOF via reductive labilization. *Chem. Sci.* **2015**, *6* (12), 7044−7048.
(43) Wang, J.-H.; Zhang, Y.; Li, M.; Yan, S.; Li, D.; Zhang, X.-M. Solvent-Assisted Metal Metathesis: A Highly Efficient and Versatile Route towards Synthetically Demanding Chromium Metal−Organic Frameworks. *Angew. Chem., Int. Ed.* **2017**, *129* (23), 6578−6582.
(44) Barsukova, M.; Sapianik, A.; Shkurenko, A.; Bonneau, M.; Bin Hemid, S.; Jin, T.; Guillerm, V.; Eddaoudi, M. Enriching Trans-metalation Routes to Stable and Highly Porous Crystals of Chromium-Based Metal−Organic Frameworks. *J. Am. Chem. Soc.* **2025**, *147* (47), 43745−43754.
(45) Yang, M.; Bao, Y.-S.; Zhou, M.-L.; Wang, S.; Cui, Y.-H.; Liu, W.; Li, L.-C.; Meng, L.-X.; Zhang, Y.-Y.; Han, Z.-B. An Efficient Bifunctional Core−Shell MIL-101(Cr)@MOF-867 Composite to Catalyze Deacetalization−Knoevenagel Tandem Reaction. *Catal. Lett.* **2023**, *153* (12), 3561−3568.
(46) Shi, L.; Kirlikovali, K. O.; Chen, Z.; Farha, O. K. Metal-organic frameworks for water vapor adsorption. *Chem.* **2024**, *10* (2), 484−503.
(47) Gong, W.; Chen, X.; Wahiduzzaman, M.; Xie, H.; Kirlikovali, K. O.; Dong, J.; Maurin, G.; Farha, O. K.; Cui, Y. Chiral Reticular Chemistry: A Tailored Approach Crafting Highly Porous and Hydrolytically Robust Metal−Organic Frameworks for Intelligent Humidity Control. *J. Am. Chem. Soc.* **2024**, *146* (3), 2141−2150.
(48) Chen, X.; Wee, L.; Alizadeh Kiapi, M.; Tampaxis, C.; Zheng, Y.; Asgari, M.; Menon, D.; Willhammar, T.; Keenan, L.; Charalambopoulou, G.; Cui, Y.; Steriotis, T. A.; Fairen-Jimenez, D., Topology-driven design of an ultraporous red MOF for high-performance hydrogen storage. *ChemRxiv* (Materials Chemistry). September *24*, **2025**. DOI (accessed 2025−09−25).

https://doi.org/10.1021/jacs.5c16581
J. Am. Chem. Soc. XXXX, XXX, XXX−XXX